Universal Behavior of the Scattering Matrix Near Thresholds in Photonics

Charles C. Wojcik,[1] Haiwen Wang,[2] Meir Orenstein,[3] and Shanhui Fan[1,*]
[1]Department of Electrical Engineering, Ginzton Laboratory, Stanford University, Stanford, California 94305, USA
[2]Department of Applied Physics, Ginzton Laboratory, Stanford University, Stanford, California 94305, USA
[3]Department of Electrical Engineering, Technion-Israel Institute of Technology, Haifa 32000, Israel

(Received 5 April 2021; accepted 7 December 2021; published 28 December 2021)

Scattering thresholds and their associated spectral square root branch points are ubiquitous in photonics. In this Letter, we show that the scattering matrix has a simple universal behavior near scattering thresholds. We use unitarity, reciprocity, and time-reversal symmetry to construct a two-parameter model for a two-port scattering matrix near a threshold. We demonstrate this universal behavior in three different optical systems, namely, a photonic crystal slab, a planar dielectric interface, and a junction between metallic waveguides of different widths.

DOI: 10.1103/PhysRevLett.127.277401

Scattering theory is the mathematical framework for describing physical systems with inputs and outputs. Originally developed to study the scattering of subatomic particles in quantum mechanics [1,2] and to design microwave circuits [3], it has more recently become important in photonics [4–19] describing processes where the inputs and outputs are optical waves.

The main object in scattering theory is the scattering matrix (S matrix), which relates the output amplitudes to the input amplitudes. The S matrix has a rich analytic structure which has been used to understand very general behavior of scattering processes. For example, poles of the S matrix have been used to develop a coupled-mode theory description of the Fano resonance in optical resonators [7–9] and in the basic modal description of waveguides [20], while zeros of the S matrix have been used to design coherent perfect absorbers [12,14] and reflectionless scattering modes [21].

Besides poles and zeros, another universal analytic feature of the S matrix is the square root branch point [1]. This branch point occurs when parameters such as frequency or angle are varied so that propagating channels (those with real phase accumulation) transition into evanescent channels (having imaginary phase accumulation). We refer to the transition point as a scattering threshold and the channels undergoing this transition (having zero phase accumulation) as threshold channels. For far-field engineering, the S matrix can be restricted to include propagating channels only, in which case the size of the S matrix changes at the threshold. However, for near-field engineering, the S matrix needs to be extended to include evanescent channels, in which case the size of the S matrix remains constant [22,23].

In photonics, this square root singularity has been observed in the context of the Rayleigh-Wood anomalies in the spectra of diffraction gratings and photonic crystals, associated with the appearance of new diffraction orders. It is well established that the origin of this square root behavior is the dispersion relation which determines the wave vector in terms of other parameters like frequency or angle [24–27]. There have also been detailed studies of the modified behavior of resonant poles in the presence of scattering thresholds [28–33]. In the absence of resonant poles, the square root singularity has recently been considered as a possible means of enhanced sensing [18,34]. Despite the theoretical and practical importance of understanding scattering thresholds, to the best of our knowledge there has not been a systematic treatment of the behavior of the S matrix at isolated scattering thresholds in photonics which fully incorporates the constraints of unitarity, reciprocity, and time-reversal symmetry.

In this Letter, we show that the square root branch point is associated with strong constraints on the entries of the S matrix, and thus the N-port S matrix has a simple universal behavior near scattering thresholds. Specifically, we argue on general grounds that at the scattering threshold, the threshold channels see a reflection coefficient of -1 and vanishing transmission coefficients [Eq. (2)]. Specializing to the two-port case (the N-port case is explained in the Supplemental Material [35]) and imposing the further constraints of unitarity, reciprocity, and time-reversal symmetry, we obtain a general two-parameter analytic model for the S matrix near a scattering threshold [Eq. (3)].

As a first example of a system with a scattering threshold, we consider a photonic crystal slab sitting on top of a perfect mirror, as shown in Fig. 1(a). We calculate the S matrix in this system using rigorous coupled wave analysis (RCWA) [36]. The photonic crystal slab couples two free-space scattering channels, $i = 1, 2$, each supporting an incoming (a_i) and outgoing (b_i) wave, as shown in Fig. 1(b). As we approach the critical frequency of the scattering threshold from above, the wave vectors associated with channel 2

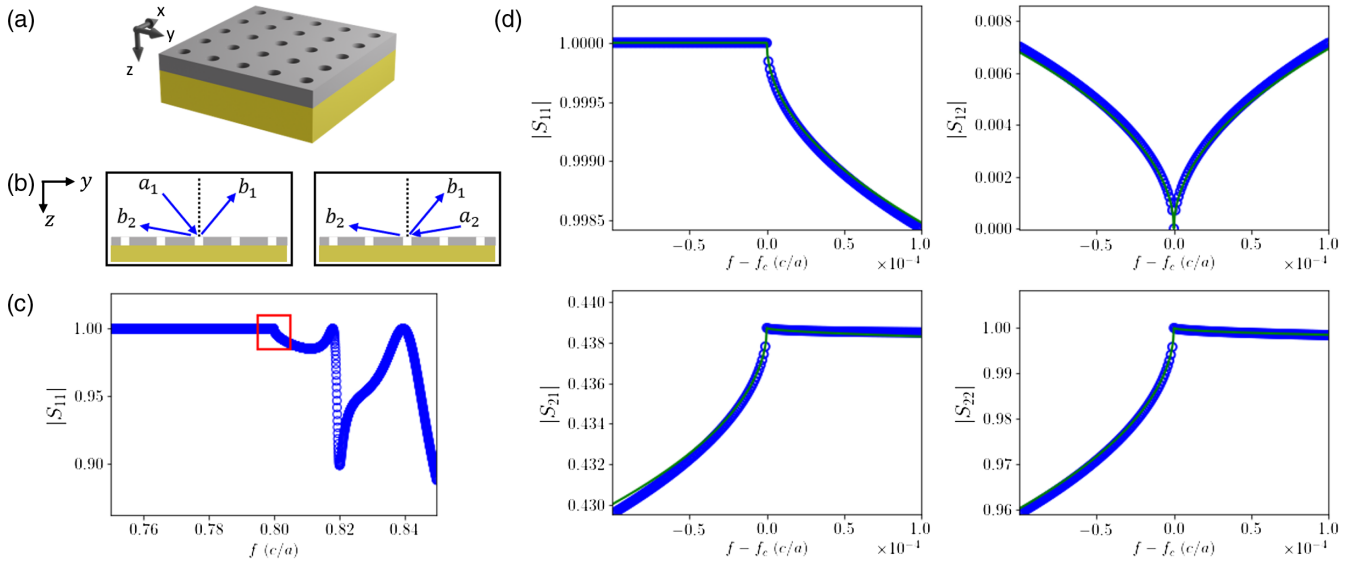

FIG. 1. A scattering threshold in a photonic crystal slab. (a) The structure is a photonic crystal slab with dielectric constant $\epsilon = 3.5$ sitting on a perfect mirror. The air holes have radius $0.2a$, where a is the lattice constant, and the slab thickness is $0.5a$. We take the wave vector to be in the yz plane and the electric field to be pointing in the x direction (transverse electric, TE). (b) The input a_1 and zeroth order output b_1 have $k_y = 0.2(2\pi/a)$. At frequencies $f > 0.8c/a$, there is a first-order diffraction channel output b_2 with $k_y = -0.8(2\pi/a)$. We additionally consider the input a_2 into this first-order channel so that we can impose reciprocity and time-reversal symmetry. (c) A portion of the reflection spectrum from channel 1 is shown, with a red box indicating the kink at the scattering threshold. (d) The magnitudes of the matrix elements of the two-channel S matrix near the threshold are shown. The circles are from simulations using RCWA [36] while the solid curve is from the two-parameter analytical model [Eq. (3)]. The parameter values for the model (defined below) are $t = 0.438$ and $g = -1.282$. The primary features of the spectrum are the kink as well as the values $S_{12} = 0$ and $|S_{22}| = 1$ at threshold.

approach an angle which is parallel to the slab. Below the critical frequency, channel 2 is evanescent in the z direction (the z component of the wave vector is imaginary). The z component of the propagation constant associated with channel 2 is

$$\beta = 2\pi\sqrt{\left(\frac{f}{c}\right)^2 - \left(\frac{-0.8}{a}\right)^2}.$$

This is the origin of the threshold square-root branch point: the threshold critical frequency $f_c = 0.8c/a$ for this diffraction order is defined by

$$\beta(f = f_c) = 0$$

so that near the critical frequency

$$\beta \approx \frac{2\pi}{c}\sqrt{2f_c(f - f_c)}.$$

The S matrix is analytic as a function of β, so the square root branch point in this case comes from this relation between β and f. In general, we will use the dispersion relations of the scattering channels to identify the critical values of the parameters associated with scattering thresholds.

In Fig. 1(c), we plot the magnitude of the reflection coefficient, $|S_{11}|$ (which relates b_1 to a_1), as a function of frequency. We see a flat response below the critical frequency, since the second channel is evanescent and all of the power is reflected into the first channel. Above the critical frequency, there are two propagating channels, and we see a typical photonic crystal spectrum with Fano resonances on a smooth background. Near the critical frequency, we see the square-root spectral kink (indicated by a red box) which is characteristic of a scattering threshold (in this case, the Rayleigh-Wood anomaly).

In Fig. 1(d), we show a closer view of the magnitude of each entry of the two-port S matrix near the critical frequency. The notable features are the square-root kink at the threshold, as well as the fact that $S_{12} = 0$ and $|S_{22}| = 1$ at threshold. As we shall see, these features are universal at scattering thresholds. The numerical data show a good fit with the two-parameter analytic model which we derive below [Eq. (3)].

Now that we have seen an example of a scattering threshold, we can provide a general analytic argument for the notable features. We consider a scattering system with N channels, each of which can be propagating, evanescent, or threshold. The transverse electric and magnetic fields in the nth channel ($1 \le n \le N$) can be expressed in terms of forward and backward traveling waves as

$$(E_n)_x(z) = a_n e^{-i\beta_n z} + b_n e^{i\beta_n z}$$
$$(H_n)_y(z) = \frac{\beta_n}{\omega\mu_0}(a_n e^{-i\beta_n z} - b_n e^{i\beta_n z}).$$

Here, β_n is the propagation constant (the z component of the wave vector), ω is the angular frequency, and μ_0 is the vacuum permeability.

We now simplify the notation by evaluating at $z = 0$ and dropping the x and y subscripts on the electric and magnetic fields. We switch to a vector notation to treat all the channels at once, so $\mathbf{E}$ and $\mathbf{H}$ are N-component vectors, and we define the characteristic impedance matrix

$$\mathbf{Z_0} = \mathrm{diag}\left(\frac{\omega\mu_0}{\beta_n}\right).$$

We can now write more simply

$$\mathbf{E} = \mathbf{a} + \mathbf{b}$$
$$\mathbf{H} = \mathbf{Z_0}^{-1}(\mathbf{a} - \mathbf{b}).$$

In addition to the characteristic impedance matrix, we also need the wave impedance matrix (Z matrix), defined by

$$\mathbf{E} = \mathbf{Z}\mathbf{H}$$

(recalling that $\mathbf{E}$ and $\mathbf{H}$ are vectors containing only transverse field components). Noting also the definition of the S matrix by the equation $\mathbf{b} = \mathbf{S}\mathbf{a}$, it follows that

$$\mathbf{S} = -(\mathbf{1} + \mathbf{Z}\mathbf{Z_0}^{-1})^{-1}(\mathbf{1} - \mathbf{Z}\mathbf{Z_0}^{-1}) \tag{1}$$

where $\mathbf{1}$ denotes the identity matrix. (See the Supplemental Material [35] for the derivation.)

We now turn our attention to the behavior exactly at the scattering threshold. We partition the channels (and therefore the matrices $\mathbf{S}$ and $\mathbf{Z}$) into three blocks, corresponding to propagating channels, threshold channels, and evanescent channels, respectively. The propagation constants of the threshold channels vanish at the critical frequency, so in our case [transverse electric (TE)] the characteristic impedance of these channels is infinite. (This can be avoided in metamaterials where $\mu = 0$ [37].) The wave impedance (including cross-impedance between channels), on the other hand, generically remains finite at the threshold. From these properties, we can show that exactly at the threshold, the S matrix takes the block form

$$\mathbf{S} = \begin{pmatrix} * & \mathbf{0} & * \\ * & \mathbf{-1} & * \\ * & \mathbf{0} & * \end{pmatrix} \tag{2}$$

(where $\mathbf{-1}$ denotes the negative identity matrix, while asterisks denote entries which are not constrained by the threshold behavior). (See the Supplemental Material [35] for the derivation, which includes Ref. [38].) In other words, the transmission from any threshold channel to any other channel (including other threshold channels) is 0, while the reflection coefficient from any threshold channel back to itself is -1.

To understand this behavior physically, we focus on the case where the input channel is a threshold channel. In our setup, at the threshold, the diverging characteristic impedance causes the transverse magnetic field to go to zero. The finite wave impedance therefore requires that the transverse electric field also vanishes; this requires the transmission coefficients $t_{mn} = S_{mn}(m \neq n)$ and reflection coefficients $r_n = S_{nn}$ to satisfy, when channel n is exactly at threshold,

$$t_{mn} = 0$$
$$r_n = -1.$$

A general form of the N-port scattering matrix containing $N(N+1)/2$ free parameters can be derived using Eq. (1) (see discussion in the Supplemental Material [35]). For simplicity, here we explicitly derive the general form for the two-port case. To the lowest order, we can assume that $\mathbf{Z}$ is constant in frequency, so that the analytic behavior of $\mathbf{S}$ comes entirely from the square root in $\mathbf{Z_0}$. Using unitarity, reciprocity, and time-reversal symmetry, we can show that $\mathbf{Z}$ is an imaginary symmetric matrix, which is therefore determined by three real parameters. (See the Supplemental Material [35] for the derivation.) The S matrix is therefore also determined by three real parameters. One of them is not physically relevant, since it corresponds to a choice of a reference plane for the propagating channel. In terms of the other two parameters, which we call t and g, the S matrix has the form

$$\mathbf{S} = \frac{1}{1 + [ig + (t/2)^2]\delta} \times \begin{pmatrix} 1 + [ig - (t/2)^2]\delta & t\delta \\ t & -1 + [ig + (t/2)^2]\delta \end{pmatrix} \tag{3}$$

where the dimensionless parameter δ is defined as the ratio of the two propagation constants,

$$\delta = \beta_2/\beta_1.$$

(see the Supplemental Material [35] for the derivation). Recall that δ has a square-root frequency dependence near the threshold. The parameter t is interpreted as the value of the transmission coefficient t_{21} at threshold ($\delta = 0$). The parameter g relates to a choice of reference plane for the threshold channel. To leading order, g does not affect $|S_{11}|$ or $|S_{12}|$, and it only affects $|S_{21}|$ and $|S_{22}|$ below the threshold, where channel 2 is evanescent and a choice

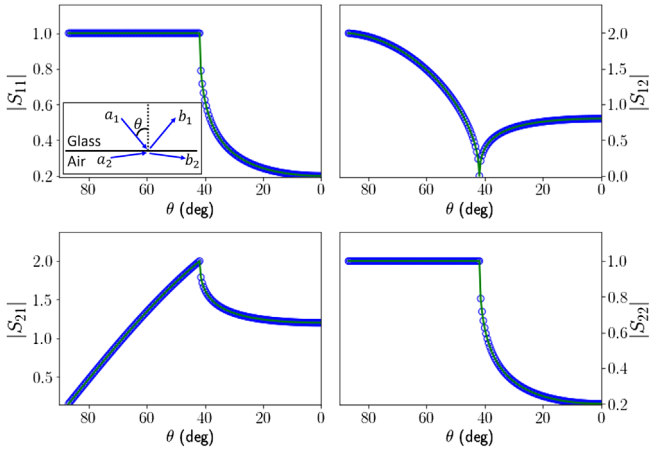

FIG. 2. A scattering threshold at a dielectric interface. An inset shows the structure, a planar dielectric interface between glass (refractive index $n = 1.5$) and air (refractive index $n = 1$), as well as the angle of incidence and the two scattering channels. The four S matrix elements are plotted as a function of incident angle. The circles are from the Fresnel equations while the solid green curves are from the two-parameter analytical model (with $t = 2$ and $g = 0$). The scattering threshold occurs at the critical angle from TIR. The agreement in this case is exact for all angles.

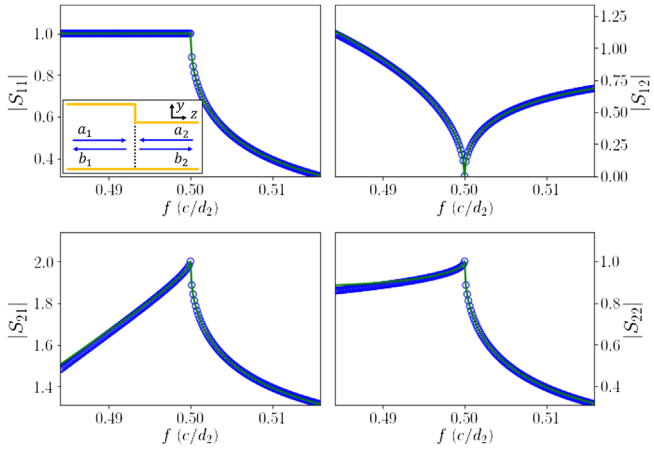

FIG. 3. A scattering threshold at a junction between two metallic waveguides of different widths. An inset shows the structure; the first waveguide has width d_1 and the second waveguide has width d_2, where $d_1 > d_2$. Accordingly, the mode of the second waveguide has a scattering threshold at the critical frequency $f = 0.5(c/d_2)$. The blue circles are numerical while the solid green curves are from the model (with $t = 2$ and $g = -0.127$).

of reference plane implements an imaginary gauge transformation [39] (see the Supplemental Material [35] for the derivation). We emphasize that this local model is only valid in the immediate vicinity of an isolated scattering threshold; other spectral features such as the resonances seen in Fig. 1(c) will decrease the range of validity of the expansion when the resonant frequency approaches the threshold frequency [40], but the expansion remains valid in a sufficiently small neighborhood of the threshold.

Now that we have an analytic model for scattering thresholds in photonics, we illustrate the universality of this model by considering two other photonic systems with scattering thresholds. First, we consider the simplest system exhibiting threshold behavior, a planar interface between two different dielectric materials, where the scattering threshold occurs at the critical angle for total internal reflection (TIR). In Fig. 2, we show the configuration and the two scattering channels. We compare our model to the known Fresnel equations that describe transmission and reflection at the interface. In this simple system, the agreement with the model is exact. Accordingly, one can view the threshold from the Fresnel equations as characteristic of the local behavior at a general scattering threshold.

For our last example, we consider a closed junction between two planar metallic waveguides of different widths, as shown in Fig. 3. In our system, the first and second waveguides have widths d_1 and d_2, respectively, and $d_1 > d_2$, so the fundamental TE mode in the first waveguide is still propagating at the cutoff frequency for the fundamental TE mode in the second waveguide. If d_1 is chosen small enough, the higher order TE modes in the first waveguide are not propagating. Because TE modes and transverse magnetic (TM) modes do not couple in this system, we can again use our two-port analytic model to describe the S matrix of the fundamental TE modes in the two waveguides at a scattering threshold. (See the Supplemental Material [35] for the details of the analysis of this system [22,41].) Again, the two-parameter model predicts the critical behavior at the scattering threshold.

A previously suggested model [26,27] captures only partially the behavior of the scattering matrix near threshold, but it does not provide an accurate description of the physical systems we consider here because it does not satisfy the physical constraint of unitarity (the deviations of the existing model from the accurate results are elaborated for all three systems in the Supplemental Material [35]). Our model which exactly satisfies the generalized unitarity relations [23] provides, in contrast, an excellent match to the accurate spectral characteristics of these systems.

When loss is added to the scattering system but the scattering channels remain lossless, the square-root kink persists but unitarity is lost (since the scattering process is lossy). This is what occurs when material loss is added to the photonic crystal slab. In contrast, when loss is added to the scattering channels but the bounded system remains lossless, the square-root kink is smoothed out but the generalized unitarity of the system remains (since energy is not lost during the scattering process but rather afterwards in the channels). This occurs at a dielectric interface when loss is added to a medium or in the metallic waveguide junction when loss is added to a waveguide. These two cases are illustrated in the Supplemental Material [35]. Our theory still applies to both cases, even for high-loss

systems; in the former case, one drops the unitarity constraints on the **Z** matrix, and in the latter case, one retains these constraints and simply inserts loss into the channel dispersion relations.

To summarize, we showed that the S matrix at a scattering threshold in photonics has a universal behavior and can be understood by a simple two-parameter model [Eq. (3)]. The argument relies on the generic property that the characteristic impedance has a square-root divergence while the wave impedance remains finite and analytic at thresholds. This universal behavior provides insight into widespread analytic features of the S matrix in photonics. The square root behavior of the S matrix at threshold may also be important for sensing applications, and the analytic model would thus be useful for understanding the constraints for engineering these thresholds.

This work is supported by a Vannevar Bush Faculty Fellowship from the U.S. Department of Defense (Grant No. N00014-17-1-3030), and by the U.S. Office of Naval Research (Grant No. N00014-20-1-2450).

*Corresponding author.
shanhui@stanford.edu

[1] J. Taylor, *Scattering Theory: The Quantum Theory of Nonrelativistic Collisions* (Dover Publications, New York, 2006).
[2] R. G. Newton, *Scattering Theory of Waves and Particles* (Springer-Verlag, Berlin, Heidelberg, 1982).
[3] D. M. Pozar, *Microwave Engineering* (John Wiley & Sons, New York, 2011).
[4] T. W. Ebbesen, H. J. Lezec, H. Ghaemi, T. Thio, and P. A. Wolff, Extraordinary optical transmission through sub-wavelength hole arrays, Nature (London) **391**, 667 (1998).
[5] S. Astilean, P. Lalanne, and M. Palamaru, Light transmission through metallic channels much smaller than the wavelength, Opt. Commun. **175**, 265 (2000).
[6] Y. Takakura, Optical Resonance in a Narrow Slit in a Thick Metallic Screen, Phys. Rev. Lett. **86**, 5601 (2001).
[7] S. Fan and J. D. Joannopoulos, Analysis of guided resonances in photonic crystal slabs, Phys. Rev. B **65**, 235112 (2002).
[8] S. Fan, W. Suh, and J. D. Joannopoulos, Temporal coupled-mode theory for the Fano resonance in optical resonators, J. Opt. Soc. Am. A **20**, 569 (2003).
[9] W. Suh, Z. Wang, and S. Fan, Temporal coupled-mode theory and the presence of non-orthogonal modes in lossless multimode cavities, IEEE J. Quantum Electron. **40**, 1511 (2004).
[10] J.-T. Shen and S. Fan, Strongly Correlated Two-Photon Transport in a One-Dimensional Waveguide Coupled to a Two-Level System, Phys. Rev. Lett. **98**, 153003 (2007).
[11] Z. Ruan and S. Fan, Temporal coupled-mode theory for Fano resonance in light scattering by a single obstacle, J. Phys. Chem. C **114**, 7324 (2010).
[12] Y. D. Chong, L. Ge, H. Cao, and A. D. Stone, Coherent Perfect Absorbers: Time-Reversed Lasers, Phys. Rev. Lett. **105**, 053901 (2010).
[13] L. Verslegers, Z. Yu, P. B. Catrysse, and S. Fan, Temporal coupled-mode theory for resonant apertures, J. Opt. Soc. Am. B **27**, 1947 (2010).
[14] W. Wan, Y. Chong, L. Ge, H. Noh, A. D. Stone, and H. Cao, Time-reversed lasing and interferometric control of absorption, Science **331**, 889 (2011).
[15] L. Ge, Y. D. Chong, and A. D. Stone, Conservation relations and anisotropic transmission resonances in one-dimensional PT-symmetric photonic heterostructures, Phys. Rev. A **85**, 023802 (2012).
[16] L. Feng, X. Zhu, S. Yang, H. Zhu, P. Zhang, X. Yin, Y. Wang, and X. Zhang, Demonstration of a large-scale optical exceptional point structure, Opt. Express **22**, 1760 (2014).
[17] S. Kruk and Y. Kivshar, Functional meta-optics and nanophotonics governed by Mie resonances, ACS Photonics **4**, 2638 (2017).
[18] H. H. Sheinfux, Y. Lumer, G. Ankonina, A. Z. Genack, G. Bartal, and M. Segev, Observation of Anderson localization in disordered nanophotonic structures, Science **356**, 953 (2017).
[19] Z. Zhao, C. Guo, and S. Fan, Connection of temporal coupled-mode-theory formalisms for a resonant optical system and its time-reversal conjugate, Phys. Rev. A **99**, 033839 (2019).
[20] W. C. Chew, *Waves and Fields in Inhomogeneous Media* (IEEE Press, New York, 1995).
[21] W. R. Sweeney, C. W. Hsu, and A. D. Stone, Theory of reflectionless scattering modes, Phys. Rev. A **102**, 063511 (2020).
[22] G. V. Eleftheriades, A. S. Omar, L. P. Katehi, and G. M. Rebeiz, Some important properties of waveguide junction generalized scattering matrices in the context of the mode matching technique, IEEE Trans. Microw. Theory Techn. **42**, 1896 (1994).
[23] R. Carminati, J. J. Sáenz, J.-J. Greffet, and M. Nieto-Vesperinas, Reciprocity, unitarity, and time-reversal symmetry of the S matrix of fields containing evanescent components, Phys. Rev. A **62**, 012712 (2000).
[24] U. Fano, The theory of anomalous diffraction gratings and of quasi-stationary waves on metallic surfaces (Sommerfelds waves), J. Opt. Soc. Am. **31**, 213 (1941).
[25] A. Hessel and A. Oliner, A new theory of Woods anomalies on optical gratings, Appl. Opt. **4**, 1275 (1965).
[26] B. Bolotovskii and A. Lebedev, On threshold phenomena in classical electrodynamics, Sov. Phys. JETP **26**, 784 (1968).
[27] A. I. Baz', I. B. Zel'dovich, and A. Perelomov, *Scattering, Reactions and Decay in Nonrelativistic Quantum Mechanics* (Israel program for scientific translations, Jerusalem, 1969).
[28] E. P. Wigner, On the behavior of cross sections near thresholds, Phys. Rev. **73**, 1002 (1948).
[29] V. Lomakin and E. Michielssen, Enhanced transmission through metallic plates perforated by arrays of subwavelength holes and sandwiched between dielectric slabs, Phys. Rev. B **71**, 235117 (2005).
[30] V. Lomakin and E. Michielssen, Transmission of transient plane waves through perfect electrically conducting plates

perforated by periodic arrays of subwavelength holes, IEEE Trans. Antennas Propag. **54**, 970 (2006).
[31] M. Navarro-Cía, M. Beruete, F. Falcone, M. Sorolla, and V. Lomakin, Negative group delay through subwavelength hole arrays, Phys. Rev. B **84**, 075151 (2011).
[32] A. Maurel, S. Félix, J.-F. Mercier, A. Ourir, and Z. E. Djeffal, Woods anomalies for arrays of dielectric scatterers, J. Eur. Opt. Soc.-Rapid Publ. **9** (2014).
[33] H. H. Sheinfux, I. Kaminer, Y. Plotnik, G. Bartal, and M. Segev, Subwavelength Multilayer Dielectrics: Ultrasensitive Transmission and Breakdown of Effective-Medium Theory, Phys. Rev. Lett. **113**, 243901 (2014).
[34] W. Chen, Ş. K. Özdemir, G. Zhao, J. Wiersig, and L. Yang, Exceptional points enhance sensing in an optical microcavity, Nature (London) **548**, 192 (2017).
[35] See Supplemental Material at http://link.aps.org/supplemental/10.1103/PhysRevLett.127.277401 for detailed derivations as well as the generalization to the N-port case and an analysis of the effect of loss.
[36] W. Jin, W. Li, M. Orenstein, and S. Fan, Inverse design of lightweight broadband reflector for relativistic lightsail propulsion, ACS Photonics **7**, 2350 (2020).
[37] O. Reshef, I. De Leon, M. Z. Alam, and R. W. Boyd, Nonlinear optical effects in epsilon-near-zero media, Nat. Rev. Mater. **4**, 535 (2019).
[38] S. Lang, *Introduction to Linear Algebra* (Springer-Verlag, New York, 1986).
[39] N. Okuma, K. Kawabata, K. Shiozaki, and M. Sato, Topological Origin of Non-Hermitian Skin Effects, Phys. Rev. Lett. **124**, 086801 (2020).
[40] A. Akimov, N. A. Gippius, and S. G. Tikhodeev, Optical fano resonances in photonic crystal slabs near diffraction threshold anomalies, JETP Lett. **93**, 427 (2011).
[41] Ş. E.Kocabaş, G. Veronis, D. A. B. Miller, and S. Fan, Modal analysis and coupling in metal-insulator-metal waveguides, Phys. Rev. B **79**, 035120 (2009).